Enhanced thermoelectric power in two-dimensional transition metal dichalcogenide monolayers

Jiang Pu,[1,*] Kaito Kanahashi,[1] Nguyen Thanh Cuong,[2] Chang-Hsiao Chen,[3] Lain-Jong Li,[4] Susumu Okada,[5] Hiromichi Ohta,[6] and Taishi Takenobu[1,7,†]

[1]*Department of Advanced Science and Engineering, Waseda University, Tokyo 169-8555, Japan*

[2]*International Center for Young Scientists (ICYS) and International Center for Materials Nanoarchitectonics (MANA), National Institute for Materials Science (NIMS), Ibaraki 305-0044, Japan*

[3]*Department of Automatic Control Engineering, Feng Chia University, Taichung 40724, Taiwan*

[4]*Physical Science and Engineering Division, King Abdullah University of Science and Technology (KAUST), Thuwal 23955-6900, Kingdom of Saudi Arabia*

[5]*Graduate School of Pure and Applied Science, University of Tsukuba, Ibaraki 305-8571, Japan*

[6]*Research Institute for Electronic Science, Hokkaido University, Sapporo 001-0020, Japan*

[7]*Kagami Memorial Laboratory for Material Science and Technology, Waseda University, Tokyo 169-0051, Japan*

(Received 9 March 2016; revised manuscript received 14 June 2016; published 27 July 2016)

The carrier-density-dependent conductance and thermoelectric properties of large-area MoS_2 and WSe_2 monolayers are simultaneously investigated using the electrolyte gating method. The sign of the thermoelectric power changes across the transistor off-state in the ambipolar WSe_2 transistor as the majority carrier density switches from electron to hole. The thermopower and thermoelectric power factor of monolayer samples are one order of magnitude larger than that of bulk materials, and their carrier-density dependences exhibit a quantitative agreement with the semiclassical Mott relation based on the two-dimensional energy band structure, concluding the thermoelectric properties are enhanced by the low-dimensional effect.

DOI: 10.1103/PhysRevB.94.014312

Thermoelectric energy conversion is one of the key technologies for energy harvesting devices to convert waste heat into electric power, and vice versa [1,2]. In particular, the Seebeck coefficient (= thermopower, S), which is the proportional constant to the voltage generation against an induced temperature gradient, is a significant factor in designing thermoelectric materials [3]. Importantly, according to the Mott equation, S is proportional to the energy derivative of the electronic density of states (DOS) at around Fermi energy (E_F); therefore, low-dimensional structures/materials are suitable for thermoelectric applications [4]. In 1993, Hicks and Dresselhaus [5,6] theoretically predicted this approach, and it was experimentally confirmed by quantum wells and quantum wires [5–9].

Recently, transition metal dichalcogenide (TMDC) monolayers, such as molybdenum disulfide (MoS_2) and tungsten diselenide (WSe_2), have attracted strong attention due to their large bandgap (1–2 eV) and atomically thin thicknesses (<1 nm) [10–14]. In addition, because of ideal quantum-well structures, their thermoelectric properties have been investigated by mechanical-exfoliated and chemical vapor deposition (CVD) grown single crystalline MoS_2 monolayers, and a remarkably large S value of $-1 \times 10^5\ \mu V\,K^{-1}$ has been reported [15–17]. Very recently, the high performance was also observed in exfoliated few-layer single-crystal WSe_2 flakes [18]. Therefore, TMDC films are promising thermoelectric materials. However, several issues remain: (i) The typical sizes of single-crystal samples are less than $10\,\mu m^2$, which are not suitable for reliable measurements. (ii) Although both p- and n-type materials are necessary for thermoelectric energy conversion, the direct comparison between them has not yet been investigated. (iii) Because of the E_F dependence of S, it is critically important to control the energy band filling, and it is conventionally tuned by chemical doping. However, precisely controllable doping methods for TMDC films have not yet been established. (iv) Most importantly, although the previous studies reported the high thermoelectric properties, the experimental evaluation of the enhancement still remains a challenge. Very recently, several theoretical studies predicted that high thermoelectric performance can be achieved in ultrathin TMDCs, which encourage the enhancement due to the low-dimensional effect [19–21].

Considering these obstacles, we focus on the electric double-layer transistors (EDLTs) of large-area TMDC monolayers. Using the CVD method, we have synthesized centimeter-scale MoS_2, $MoSe_2$, and WSe_2 monolayers and have fabricated their EDLTs, in which the dielectric layers of transistors are replaced with electrolytes [22–26]. Importantly, owing to the high specific capacitance of EDLs ($1-10\,\mu F\,cm^{-2}$), EDLTs can continuously increase the carrier density up to $5 \times 10^{13}\ cm^{-2}$, which results in the tuning of the transistor polarity between p and n type [24–27]. Moreover, similar to the single-crystal samples, the CVD-grown TMDC-EDLTs achieved a high carrier mobility ($\sim 100\,cm^2\,V^{-1}\,s^{-1}$) and on/off ratio ($\sim 10^6$), providing the possible high thermoelectric performance [26].

Here, we investigate the thermoelectric properties of CVD-grown large-area MoS_2 and WSe_2 monolayers by employing EDL gating. Because of the electrostatic doping of EDLTs, we precisely controlled both the E_F and the S in n-type MoS_2. Moreover, we continuously tuned S from p to n type in ambipolar WSe_2 EDLTs. Due to the ultimately thin structure, the large $|S|$ ($>200\,\mu V\,K^{-1}$) and power factor

*hokoh.apple@fuji.waseda.jp
†takenobu@waseda.jp

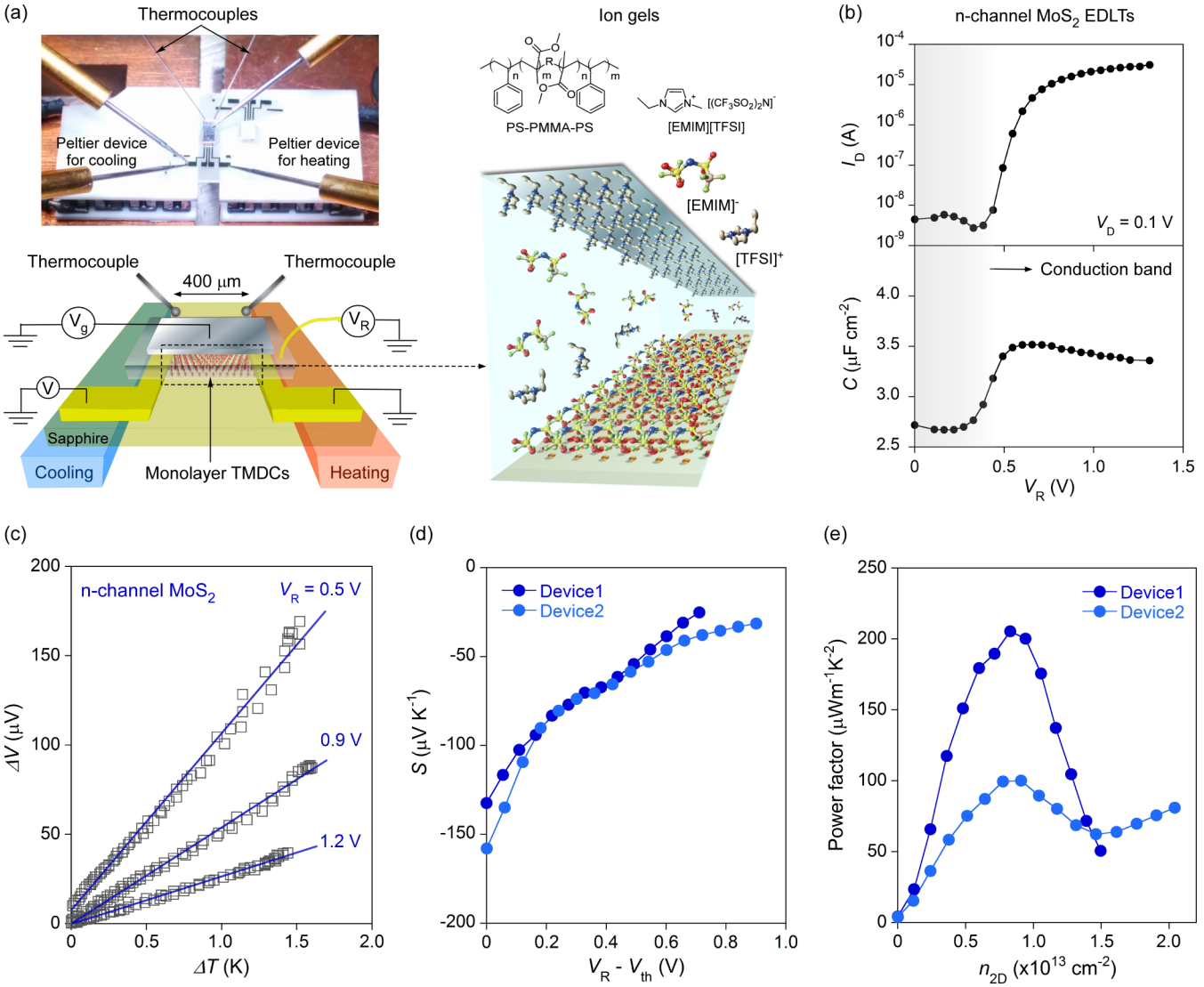

FIG. 1. Thermopower measurement in MoS_2 monolayer EDLTs. (a) A schematic depiction and an optical image of the thermopower measurement system. The ion-gel-gated EDLTs are placed on two Peltier devices, and the temperature difference (ΔT) is monitored by two thermocouples. The conceptual diagram illustrates the ionic liquid, polymer, and electrostatic doping by the EDLTs. A reference electrode is employed to estimate the voltage drop on the MoS_2 interface. (b) Transfer and capacitance-voltage characteristics of the MoS_2 EDLTs. (c) The thermoelectromotive force (ΔV) and ΔT profile is presented with a reference voltage (V_R) application. The gray blanks indicate the measured data, and the solid lines exhibit their linear fitting. (d) The measured thermopower S vs $V_R - V_{th}$ is shown, indicating the modulation of S against CB filling. Two different MoS_2 devices are shown for evaluating the S. (e) The carrier-density-dependent power factor ($S^2 \cdot \sigma$, where σ is electrical conductivity) is displayed in two devices.

($>200\,\mu W\,m^{-1}K^{-2}$) were observed in both MoS_2 and WSe_2, representing the myriad possibilities for TMDC-based large-area thermoelectric applications. We additionally investigated the origin of this enhancement by the Mott relation based on the two-dimensional (2D) energy band structure, which is calculated by the density functional theory (DFT). As a result, we quantitatively clarified the physical mechanism of the enhancement as the low-dimensional effect in the thermopower properties.

To demonstrate field-effect-modulated thermoelectric properties, first, highly uniform MoS_2 monolayer films were grown on sapphire substrates using the CVD technique, and the synthesized films were spectroscopically characterized [23] (Supplemental Material Fig. S1 [28]). The MoS_2 EDLTs with ion gels, which are a mixture of an ionic liquid and a triblock copolymer, were constructed on these large-area MoS_2 monolayers [22] (Supplemental Material [28]). Figure 1(a) schematically illustrates the device configuration and the conceptual diagram of the electrostatic doping by the EDLTs. Importantly, we introduced a long channel length of 400 μm, which are crucial to induce a clear temperature gradient for reliable thermopower measurements. Notably, the quasireference electrode was inserted into gel films to measure the effective voltage contribution on the interface between the MoS_2 and the ion gels. Because the applied gate voltage was partially consumed on the interface of the gate electrode, measuring the precise voltage drop at the MoS_2 interface is important to control the E_F of materials [29,30].

Figure 1(b) exhibits the reference-electrode voltage V_R, dependence of drain current, and capacitance. An n-type transistor characteristic and a high specific capacitance for the EDLs on the MoS_2 interface (several microfarads per square centimeter) were obtained; these results are consistent with previous reports [22–27]. Using the measured capacitances, the field-effect mobility μ of $32\,cm^2\,V^{-1}\,s^{-1}$ was calculated, indicating the superior transport properties of the CVD-grown MoS_2. Interestingly, the V_R dependence of capacitance exhibits a step function shape, as represented in the bottom panel of Fig. 1(b). This behavior can be explained by a series of connections between two different capacitances on the MoS_2 surfaces, the geometrical capacitance (C_g) and the quantum capacitance (C_q) [29,30]. The measured total specific capacitance (C_t) is dominated by C_q when E_F is within the material bandgap; conversely, when E_F is within the conduction band (CB), both C_g and C_q contribute to C_t. Importantly, because C_q is proportional to the DOS around E_F, this step capacitance-V_R relationship strongly suggests the stairlike energy dependence of the DOS in our MoS_2 film, which is a signature of 2D materials.

In order to investigate the S of monolayer MoS_2, as shown in Fig. 1(a), the fabricated EDLTs were placed between two Peltier devices, of which one is for heating and the other for cooling devices. Two thermocouples (K type, $\phi = 100\,\mu m$) were placed on both edges of the channel to monitor the temperature difference (ΔT). Because of the long channel, ΔT reached 1.5 K. The thermoelectromotive force (ΔV) and ΔT values were simultaneously measured with V_R application at room temperature. Figure 1(c) presents the $\Delta V - \Delta T$ curves at various V_R, in which the linear relationship clearly proves the excellent reliability of these measurements. It is noted that the linearity of the $\Delta V - \Delta T$ slope was dramatically degraded when the channel resistance was high, suggesting the adverse effects of metal/MoS_2 contacts. Therefore, to prevent these negative effects, we derived S from the linear fitting of the $\Delta V - \Delta T$ curve and accepted only the results with determination coefficients that were greater than 0.98. As a result, we mostly obtained reliable behavior above the threshold voltage (V_{th}) of the EDLTs. Figure 1(d) shows the V_R dependence of the S for two different MoS_2 EDLTs. The derived S is displayed as a function of $V_R - V_{th}$, indicating that the data are plotted from CB edge and that the horizontal axis correlates with the E_F shift. Obviously, S is controlled by the EDL gating, and we obtained a maximum $|S|$ value of $160\,\mu V\,K^{-1}$ at around the CB edge, which qualitatively agrees with the energy derivative of the 2D DOS.

To further evaluate the thermoelectric performance of monolayer MoS_2, we also calculated the thermoelectric power factor $S^2 \cdot \sigma$. The electrical conductivity σ was directly converted from measured drain current I_D by using the equation $\sigma = (L \cdot I_D)/(W \cdot V_D \cdot t)$, where the L is the channel length, the W is the channel width, the V_D is the drain voltage, and t is the thickness of monolayer films [23–26]. It should be strongly emphasized that the power factor has to be optimized to maximize the electric power output of thermoelectric devices. Consequently, this is a key parameter for applications. However, it is widely known that there is a tradeoff between $|S|$ and σ in terms of carrier density n. Although σ is almost linearly proportional to n, $|S|$ decreases with increasing n [2]. Therefore, it is necessary to maximize $S^2 \cdot \sigma$ by tuning n. Figure 1(e) exhibits the sheet carrier density n_{2D} dependence of the power factor. We estimated n_{2D} from the equation $n_{2D} = \int C_t \cdot (V_R - V_{th})/e$, where e is the elementary charge. Most importantly, we continuously controlled the power factor, and a high power factor of $\sim 200\,\mu W\,m^{-1}K^{-2}$ was obtained above the n_{2D} of $1 \times 10^{13}\,cm^{-2}$, which is approximately two times higher than those of graphene ($\sim 100\,\mu W\,m^{-1}K^{-2}$) [31,32] and carbon nanotube ($\sim 100\,\mu W\,m^{-1}K^{-2}$) [33,34]. It should be noted that, although the thermopower is reproducible among samples, the power factor is strongly sample dependent due to the variation of the σ in each device, which might be caused by adverse effects of film quality, such as grain boundaries and/or defects originated from sulfur vacancy (also see Supplemental Material Fig. S2 [28]).

To explore p-type thermoelectric materials, we focused on monolayer WSe_2. Large-area WSe_2 monolayer films were also synthesized using the CVD system, and the film quality was confirmed by spectroscopic methods [25] (Supplemental Material Fig. S3 [28]). Figure 2(a) shows the transfer and capacitance-V_R characteristics of the WSe_2 EDLTs. An obvious ambipolar transport with an on/off ratio of 10^5 for both p- and n-type transports was observed, which is direct evidence of continuous E_F control from valence band (VB) to CB. In addition, the μ reached $53\,cm^2\,V^{-1}\,s^{-1}$ for holes and $8\,cm^2\,V^{-1}\,s^{-1}$ for electrons, which is consistent with previous results [25]. Moreover, similar to the MoS_2, steplike capacitance-V_R behavior was observed, reflecting the DOS of the monolayer WSe_2. Importantly, in both the transfer and the capacitance measurements, the symmetric stairlike V_R dependence was collected, and the V_R difference between two thresholds agreed with the bandgap of WSe_2 (~1.65 eV), as shown in the shadow area of Fig. 2(a).

Figure 2(b) displays the $\Delta V - \Delta T$ curve, and as the V_R changed from negative to positive, the sign of ΔV reversed, indicating the change in the predominant carrier type from holes to electrons. We derived S from the linear fitting of Fig. 2(b), and the resulting V_R dependence of S for three different WSe_2 EDLTs is revealed in Fig. 2(c). Importantly, both positive and negative S values are clearly observed in the ambipolar WSe_2 EDLTs, and this is the first demonstration of controlling p- and n-type thermoelectric properties in monolayer TMDCs. The obtained maximum $|S|$ value reached $380\,\mu V\,K^{-1}$ for the p-type and $250\,\mu V\,K^{-1}$ for the n-type WSe_2, which are larger than graphene ($<200\,\mu V\,K^{-1}$) [31,32], carbon nanotubes ($<200\,\mu V\,K^{-1}$) [33,34], and Bi_2Te_3 ($\sim 200\,\mu V\,K^{-1}$) [35]. Furthermore, as shown in Fig. 2(d), we also calculated a maximum power factor of $300\,\mu W\,m^{-1}\,K^{-2}$ for the p type and $100\,\mu W\,m^{-1}\,K^{-2}$ for the n type, indicating the potential ability of CVD-grown WSe_2 as a promising thermoelectric material. In addition, we evaluated the reproducibility of the obtained power factor value (Supplemental Material Fig. S4 [28]). Similar to MoS_2, although the thermopower is reproducible, the power factor shows the variation due to the sample-dependent σ, and the maximum value is in the range from 200 to $300\,\mu W\,m^{-1}\,K^{-2}$ for p-type WSe_2. Importantly, the highest power factor is obtained at $|n_{2D}|$ of $\sim 1.5 \times 10^{13}\,cm^{-2}$, highlighting the great advantage of EDL gating.

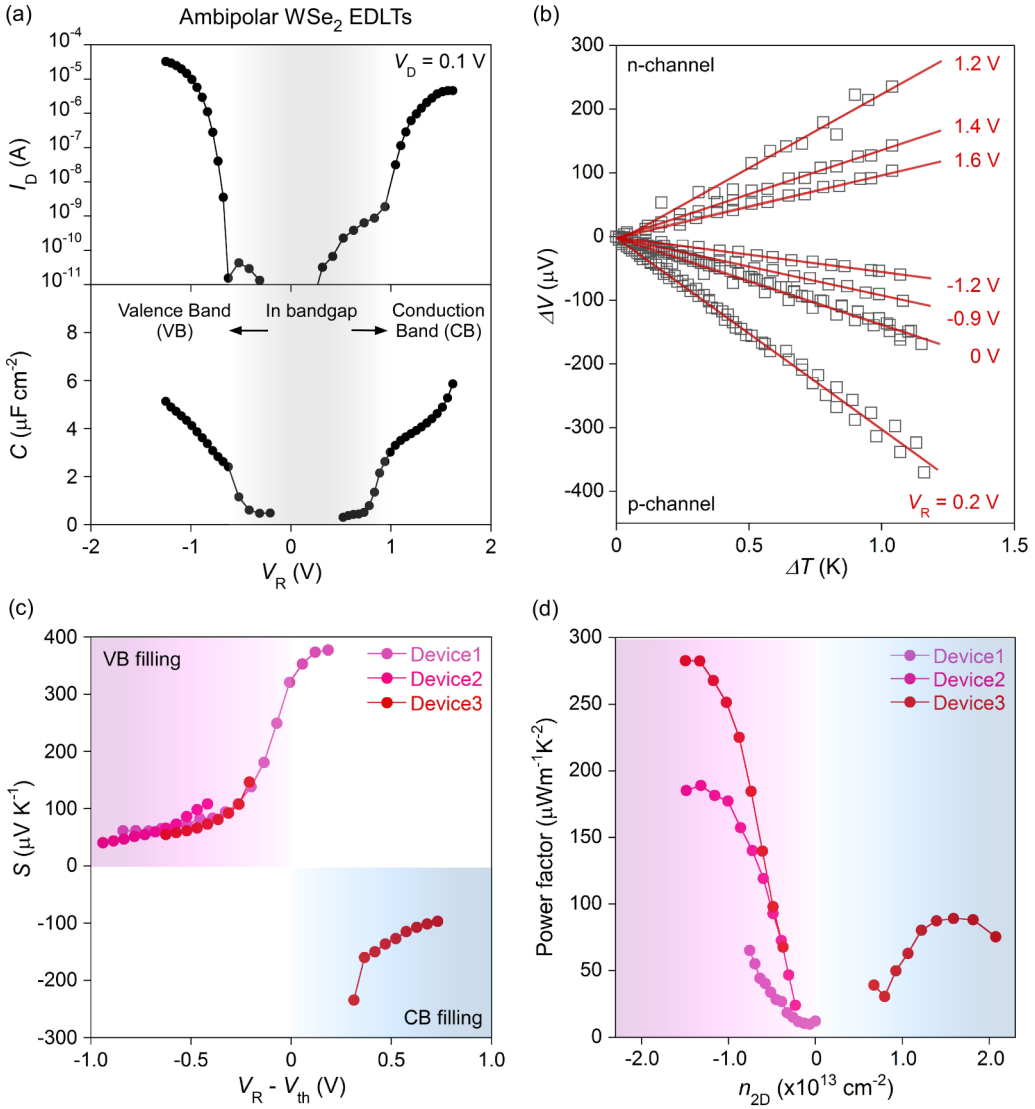

FIG. 2. Electric-filed-modulated thermopower in WSe_2 monolayer EDLTs. (a) Transfer and capacitance-voltage characteristics of the WSe_2 EDLTs. The step-function-like capacitance behavior reflects the continuous VB and CB filling, and the voltage gap between two thresholds corresponds to the bandgap of WSe_2. (b) The $\Delta V - \Delta T$ characteristic for tuning V_R. The sign inversion of ΔV is due to the change in the predominant carrier type from holes to electrons. (c) The measured S is represented as a function of $V_R - V_{th}$ for both p- and n-type WSe_2, which is attributed to VB and CB fillings, respectively. The results of three WSe_2 devices with different filling levels are shown. (d) The carrier-density-dependent power factor is exhibited for three devices.

It is already established that 2D materials exhibit higher thermoelectric properties than those of three-dimensional (3D) bulks because, according to the Mott equation, S is proportional to the energy derivative of the DOS at around E_F, and the stairlike energy dependence of the DOS of 2D materials leads to a larger S. This motivated our study in ideal quantum wells of TMDC monolayers [5–9]. In particular, several theoretical studies predict the enhancement of thermoelectric properties in TMDCs as decreasing layer thickness [19–21]. Owing to the increased valley degeneracy at the band edge, mono- and/or few-layer TMDCs show significantly increased σ, resulting in the enhancement of the power factor at $|n_{2D}|$ up to 1.0×10^{13} cm^{-2}. The relevant calculations demonstrated that ultrathin TMDCs can achieve 5–10 times larger increasing of the power factor than that of bulk samples. To confirm such low-dimensional effects, we compared our results with those of bulk materials. The comparison between large-area 2D monolayers and 3D bulks is summarized in Figs. 3(a) and 3(b), representing various semiconducting TMDC bulks, MoS_2 monolayers, and WSe_2 monolayers by black, blue, and red symbols, respectively [36–41]. We selected only large-area samples and excluded tiny single-crystal films. As shown in Fig. 3(a), the $|S|$ of the bulk samples is comparable with the results of the monolayer samples. However, if we focus on the samples with similar $|S|$, the σ of the 2D monolayers is a few orders of magnitude greater than that of the 3D bulks. Due to the tradeoff behavior between $|S|$ and σ, these results strongly suggest a larger $|S|$ in monolayer forms. Moreover, the higher thermoelectric properties in large-area monolayers are clarified in Fig. 3(b). Owing to the superior σ at comparable $|S|$, the power factor of the 2D monolayers is one order of magnitude larger than that of the 3D bulks, which is good agreement with

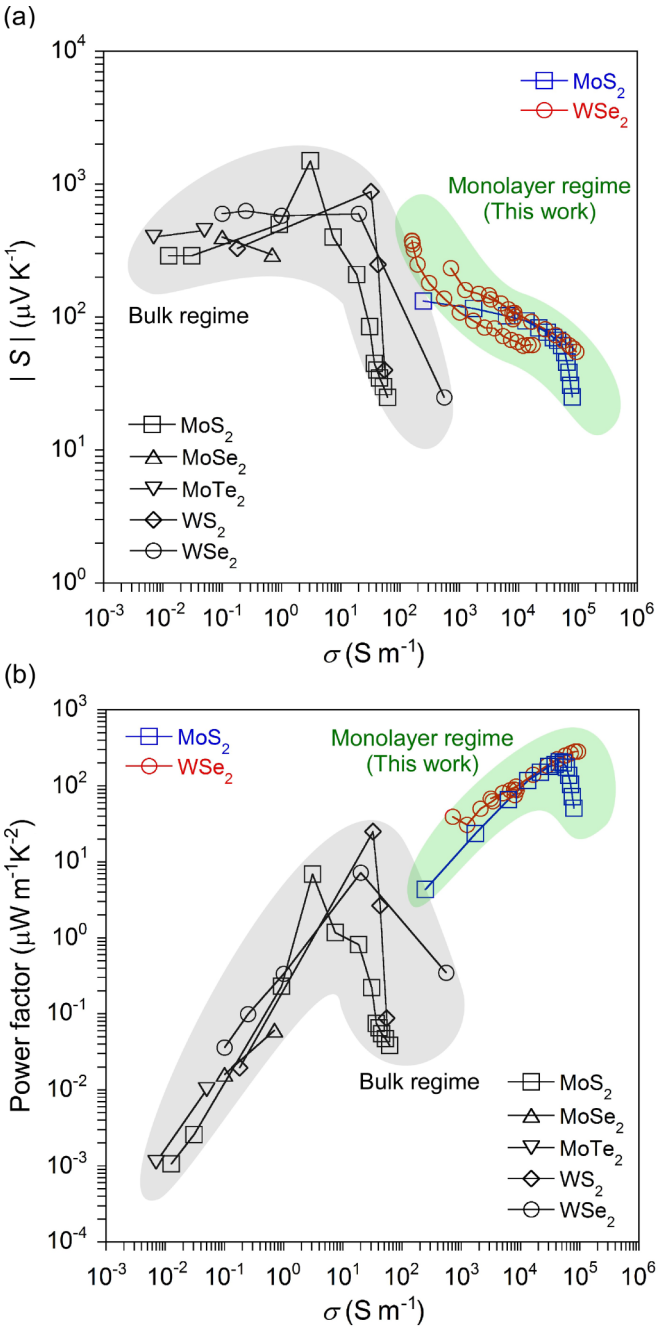

FIG. 3. Evaluation of thermoelectric properties. (a) The comparison of $|S|$ between various semiconducting TMDC bulks (gray area) and large-area monolayers (green area) is plotted against σ. The obtained data in this paper are represented by red circles for WSe_2 and by blue squares for MoS_2. The literature results for bulk materials are summarized in the black symbols [36–41]. (b) The power factor vs σ is exhibited for reported bulks (gray area) and large-area monolayers (green area) [36–41]. A significant enhancement in the 2D monolayer forms results in a power factor that is one order of magnitude larger than that in the 3D bulk forms.

theoretical predictions [19–21]. These results directly clarify the low-dimensional effect in layered TMDCs, opening up a route for high-performance thermoelectric applications.

Furthermore, we addressed the dimensionless figure of merit $ZT = S^2 \cdot \sigma \cdot T \cdot \kappa^{-1}$, where Z and κ are the figure of merit and the thermal conductivity. Although the κ of polycrystalline monolayers has not yet been established, several theoretical and experimental investigations of the in-plane κ of single-crystalline WSe_2 and MoS_2 monolayers have been reported. These κ values range from 1 to 50 $W\,m^{-1}\,K^{-1}$ at room temperature [42–45]. However, we consider that the κ of polycrystalline monolayers is smaller than that of single-crystalline monolayers because of the effects from domain/grain boundaries, and we would rather use the κ of large-area bulk samples. Very recently, the κ of polycrystalline MoS_2 films (thickness of >100 nm) have been measured, and its value is ranging from 0.5 to 1.5 $W\,m^{-1}K^{-1}$ [46,47]. If we apply these results into our polycrystalline samples, the derived ZT is up to 0.1, suggesting that the measurement of κ in polycrystalline monolayers is an important future issue.

Although the mechanism of the enhancement is qualitatively explained by the low-dimensional effect, we compared our results with those of theoretical calculations for quantitative arguments. In general, S can be expressed by the following Mott equation [4]:

$$S = -\frac{\pi^2 k_B^2 T}{3e} \cdot \frac{1}{D(E)} \cdot \frac{dD(E)}{dE}\bigg|_{E=E_F}, \quad (1)$$

where k_B and $D(E)$ are the Boltzmann constant and DOS at around E_F, respectively. Therefore, we performed the energy band calculation of monolayer WSe_2 and MoS_2 by the DFT method (see Supplemental Material [28]) and the effective screening medium (ESM) scheme [48,49]. Importantly, in TMDC monolayers, it is not clear whether or not we can apply a rigid band picture. Therefore, we need to calculate the energy dependence of both the DOS and the C_q. Figure 4(a) presents the structure of monolayer TMDCs for theoretical calculations. The lattice parameters were 3.321 Å for WSe_2 and 3.177 Å for MoS_2. The schematic representation of the ESM-DFT model is also shown in Fig. 4(a). Figures 4(b) and 4(c) indicate the calculated DOS and C_q for both WSe_2 and MoS_2. Here, C_q was estimated based on two approximations: (i) The fixed-band approximation: We calculated the energy dependence of the DOS using the DFT model. The C_q can be evaluated from the DOS of the neutral system

$$C_q(V) = \frac{1}{V_q}\int_0^{ev} D(E)dE. \quad (2)$$

The above definition assumes that the bias voltage V_q is referenced to the difference in the E_F and the maximum VB/minimum CB level. In this approximation, it is assumed that the charging or discharging simply changes the Fermi occupation of an otherwise fixed DOS of system [48]. (ii) Effective screening approximation: The WSe_2 and MoS_2 systems were charged with $+Q$ (hole doping) or $-Q$ (electron doping) to simulate the EDLs. The relaxed energy band of the charged system was calculated using the ESM-DFT scheme, and the C_q is evaluated using the following formula: $C_q = \pm Q/V_q$ [49]. The bottom panels of Figs. 4(b) and 4(c) display the difference between fixed-band and ESM-DFT calculations, which directly reflect the charging effects in 2D band structures. Because of the obvious difference between

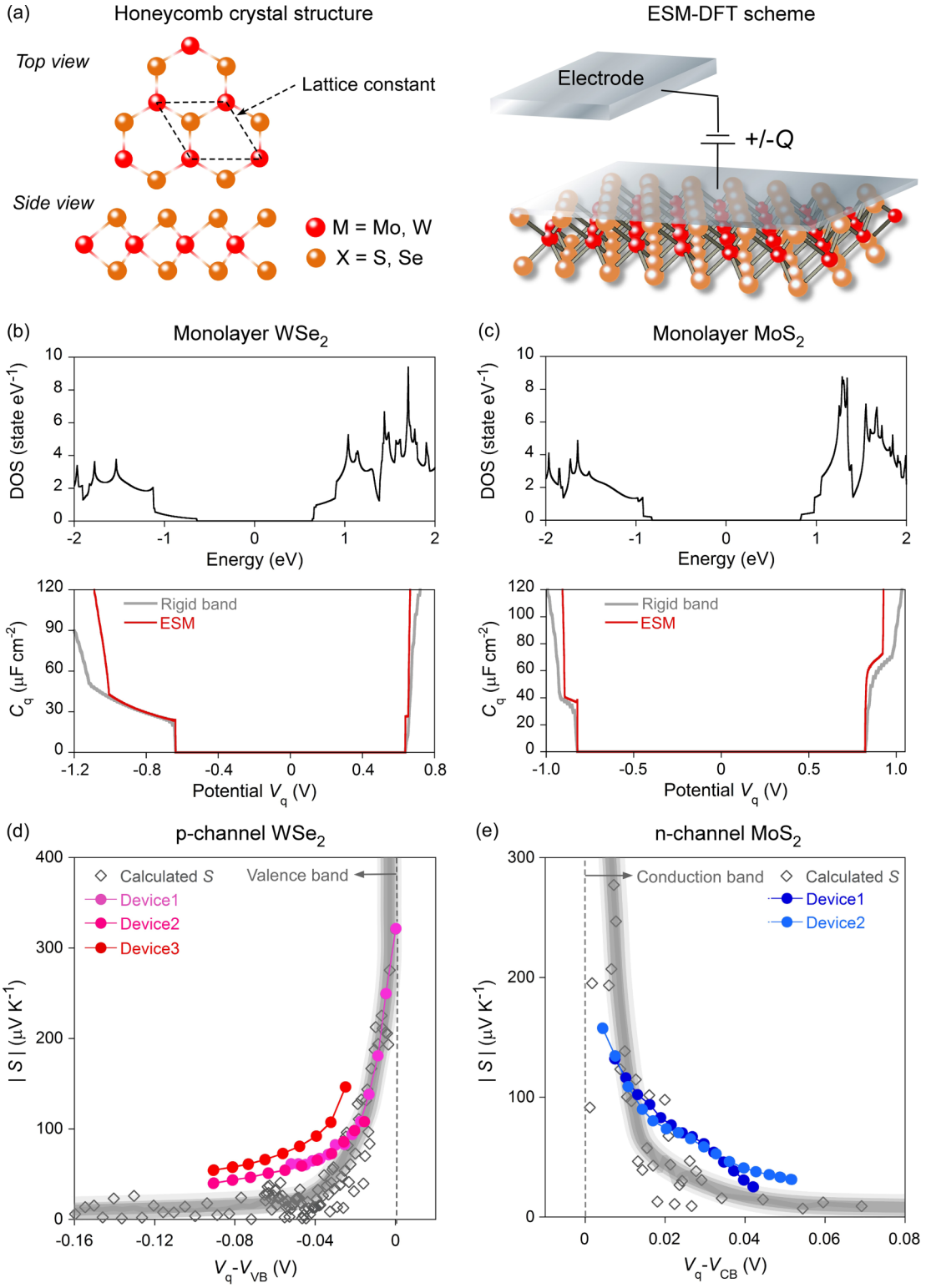

FIG. 4. Experimental and theoretical evidence showing 2D thermopower. (a) The schematics of the atomic geometry of the monolayer TMDCs and ESM model based on the DFT for the DOS and quantum capacitance C_q calculations. The relaxed energy band of charged system is calculated for the hole $(+Q)$ and the electron $(-Q)$ accumulations. (b) and (c) The calculated DOS (top) and C_q (bottom) for WSe_2 and MoS_2, respectively. Note that the V_q $(= \pm Q/C_q)$ describes the potential at each Fermi level (E_F), i.e., the required potential for shifting E_F. The C_q is displayed with the results of rigid band (gray) and ESM model (red). (d) The calculated S by the Mott equation for p-type WSe_2 is shown as a function of $V_q - V_{VB}$, where V_q is plotted from the VB edge (V_{VB}). The S (gray diamonds) is calculated by the direct derivative of C_q derived from the ESM-DFT scheme. The experimental results for the three WSe_2 EDLTs are represented by red symbols, which reasonably agreed with the theoretical data (shadow area). (e) The calculated $|S|$ for n-type MoS_2 is plotted from the CB edge of $V_q - V_{CB}$. The measured $|S|$ for two devices, shown in blue symbols, agree with the theoretical behavior (shadow area).

two results, we adopted the calculated data by the ESM-DFT model for the estimation of theoretical S, indicating that the rigid band picture is not applicable to monolayer TMDCs.

To compare the calculated results with those of experiments, we need to translate the applied V_R to the E_F shift. Because the n_{2D} can be derived from both calculated C_q ($= \pm Q/V_q$) and measured C_t [$= n_{2D}/(V_R - V_{th})$], the experimental V_q can be derived by $(C_t/C_q) \times (V_R - V_{th})$ when $Q = n_{2D}$. Therefore, by considering the linear relationship between DOS and C_q, the Mott equation can be converted to following equation:

$$S = -\frac{\pi^2 k_B^2 T}{3e} \cdot \frac{1}{C_q(V)} \cdot \left. \frac{dC_q(V)}{dV} \right|_{V=V_q}. \quad (3)$$

Using this equation, the Fermi-level dependence of the theoretical S can be calculated for the 2D band. Figure 4(d) represents the comparison of S between the theoretical and the experimental behavior of p-type monolayer WSe_2. The derived S for all calculated C_q using Eq. (3) and experimental S are summarized in Fig. 4(d). Note that the numerical variation of S obtained by the direct derivative of C_q is ascribed to the fine energy resolution ($\sim$3 meV) arising from the k-point mesh used here. The derivative of C_q under the energy mesh of 10 meV causes the numerical instability for the resultant S. In particular, the shadow area in Fig. 4(d) represents the middle value of the calculated S, reflecting the theoretical behavior as VB filling. Interestingly, the experimental S against the E_F shift shows agreement with the calculated S. Moreover, as shown in Fig. 4(e), to evaluate the n-type monolayer MoS_2, we also performed the same calculations, and the shadow area of Fig. 4(e) represents the theoretical value derived from the Mott equation. Consequently, similar to WSe_2, the experimental S is explained by the calculated curve. To further encourage the significance of our evaluation, we also calculated the theoretical S by the semiclassic Boltzmann transport theory and the Mott relation with a rigid band model for both WSe_2 and MoS_2 (Supplemental Material [28]). Although the calculated S by the rigid band model is qualitatively consistent with the experimental results, they are quantitatively inconsistent, especially for the n-type MoS_2, indicating a significant charging effect in monolayer TMDCs (Supplemental Material Fig. S5 [28]). These comparisons between the theoretical and the experimental results obviously reveal that the obtained high S in our large-area films originates from the 2D band structure of the monolayer TMDCs.

In summary, we demonstrated the carrier-density-dependent thermoelectric properties of large-area WSe_2 and MoS_2 monolayers by EDLT gating. We realized continuous modulation of positive and negative S in WSe_2 and tuned negative S in MoS_2. Moreover, the large $|S|$ ($>200\,\mu V\,K^{-1}$) and power factor ($>200\,\mu W\,m^{-1}\,K^{-2}$) were obtained with optimized carrier densities, resulting in notable enhancement of thermoelectric performance compared with that of bulks. Finally, we investigated the origin of the large S through a quantitative comparison between the theoretical Mott relation and the experimental results, and by the ESM-DFT method, the experimental S reasonably agrees with the theoretical calculations. These results strongly indicate that monolayer TMDCs are a new 2D platform for discovering high-performance large-area thermoelectric devices.

This paper was supported by the Funding Program for the Next Generation of World-Leading Researchers and Grants-in-Aid from the Ministry of Education, Culture, Sports, Science and Technology (MEXT) (Grants No. 16K13618, No. 26107533, No. 26102012, and No. 25000003) (T.T.) and the Leading Graduate Program in Science and Engineering, Waseda University from MEXT (J.P. and K.K.). J.P. was also supported by the Research Fellowship for Young Scientists from JSPS. L.J.L. acknowledges support from KAUST (Saudi Arabia), the Ministry of Science and Technology, the Taiwan Consortium of Emergent Crystalline, Academia Sinica, and the Asian Office of Aerospace Research and Development (AOARD)-134137 (USA). H.O. was supported by Japan Society for the Promotion of Science-Grants-in-Aid for Scientific Research (JSPS-KAKENHI) (Grants No. 25246023 and No. 25106007) and the Asahi Glass Foundation. This paper was also supported in part by the Network Joint Research Center for Materials and Devices. S.O. was supported by JSPS-KAKENHI (Grants No. 25246010, No. 16H00898, and No. 16H06331).

[1] F. J. DiSalvo, Science **285**, 703 (1999).
[2] G. J. Snyder and E. S. Toberer, Nat. Mater. **7**, 105 (2008).
[3] T. J. Seebeck, Abh. K. Akad. Wiss. Berlin, 265 (1823).
[4] M. Cutler and N. F. Mott, Phys. Rev. **181**, 1336 (1969).
[5] L. D. Hicks and M. S. Dresselhaus, Phys. Rev. B **47**, 12727 (1993).
[6] L. D. Hicks, T. C. Harman, X. Sun, and M. S. Dresselhaus, Phys. Rev. B **53**, R10493(R) (1996).
[7] M. S. Dresselhaus, G. Chen, M. Y. Tang, R. Yang, H. Lee, D. Wang, Z. Ren, J.-P. Fleurial, and P. Gogna, Adv. Mater. **19**, 1043 (2007).
[8] H. Ohta, S.-W. Kim, Y. Mune, T. Mizoguchi, K. Nomura, S. Ohta, T. Nomura, Y. Nakanishi, Y. Ikuhara, M. Hirano, H. Hosono, and K. Koumoto, Nat. Mater. **6**, 129 (2007).
[9] H. Ohta, T. Mizuno, S. Zheng, T. Kato, Y. Ikuhara, K. Abe, H. Kumomi, K. Nomura, and H. Hosono, Adv. Mater. **24**, 740 (2012).
[10] K. S. Novoselov, D. Jiang, F. Schedin, T. J. Booth, V. V. Khotkevich, S. V. Morozov, and A. K. Geim, Proc. Natl Acad. Sci. USA **102**, 10451 (2005).
[11] V. Podzorov, M. E. Gershenson, C. Kloc, R. Zeis, and E. Bucher, Appl. Phys. Lett. **84**, 3301 (2004).
[12] K. F. Mak, C. Lee, J. Hone, J. Shan, and T. F. Heinz, Phys. Rev. Lett. **105**, 136805 (2010).
[13] W. Zhao, Z. Ghorannevis, L. Chu, M. Toh, C. Kloc, P.-H. Tan, and G. Eda, ACS Nano **7**, 791 (2013).
[14] Q. H. Wang, K. Kalantar-Zadeh, A. Kis, J. N. Coleman, and M. S. Strano, Nat. Nanotechnol. **7**, 699 (2012).
[15] M. Buscema, M. Barkelid, V. Zwiller, H. S. J. van der Zant, G. A. Steele, and A. Castellanos-Gomez, Nano Lett. **13**, 358 (2013).
[16] J. Wu, H. Schmidt, K. K. Amara, X. Xu, G. Eda, and B. Ozyilmaz, Nano Lett. **14**, 2730 (2014).

[17] L. Dobusch, M. M. Furchi, A. Pospischil, T. Mueller, E. Bertagnolli, and A. Lugstein, Appl. Phys. Lett. **105**, 253103 (2014).
[18] M. Yoshida, T. Iizuka, Y. Saito, M. Onga, R. Suzuki, Y. Zhang, Y. Iwasa, and S. Shimizu, Nano Lett. **16**, 2061 (2016).
[19] D. Wickramaratne, F. Zahid, and R. K. Lake, J. Chem. Phys. **140**, 124710 (2014).
[20] W. Huang, X. Luo, C. K. Gan, S. Y. Quek, and G. Liang, Phys. Chem. Chem. Phys. **16**, 10866 (2014).
[21] J. Hong, C. Lee, J.-S. Park, and J. H. Shim, Phys. Rev. B **93**, 035445 (2016).
[22] J. Pu, Y. Yomogida, K.-K. Liu, L.-J. Li, Y. Iwasa, and T. Takenobu, Nano Lett. **12**, 4013 (2012).
[23] Y.-H. Lee, X.-Q. Zhang, W. Zhang, M.-T. Chang, C.-T. Lin, K.-D. Chang, Y.-C. Yu, J. T.-W. Wang, C.-S. Chang, L.-J. Li, and T.-W. Lin, Adv. Mater. **24**, 2320 (2012).
[24] Y.-H. Chang, W. Zhang, Y. Zhu, Y. Han, J. Pu, J.-K. Chang, W.-T. Hsu, J.-K. Huang, C.-L. Hsu, M.-H. Chiu, T. Takenobu, H. Li, C.-I. Wu, W.-H. Chang, A. T. S. Wee, and L.-J. Li, ACS Nano **8**, 8582 (2014).
[25] J.-K. Huang, J. Pu, C.-L. Hsu, M.-H. Chiu, Z.-Y. Juang, Y.-H. Chang, W.-H. Chang, Y. Iwasa, T. Takenobu, and L.-J. Li, ACS Nano **8**, 923 (2014).
[26] C.-H. Chen, C.-L. Wu, J. Pu, M.-H. Chiu, P. Kumar, T. Takenobu, and L.-J. Li, 2D Mater. **1**, 034001 (2014).
[27] Y. Zhang, J. Ye, Y. Matsuhashi, and Y. Iwasa, Nano Lett. **12**, 1136 (2012).
[28] See Supplemental Material at http://link.aps.org/supplemental/10.1103/PhysRevB.94.014312 for spectroscopic characterizations of samples, device distribution, and computational details of theoretical calculations.
[29] Y. Yomogida, J. Pu, H. Shimotani, S. Ono, S. Hotta, Y. Iwasa, and T. Takenobu, Adv. Mater. **24**, 4392 (2012).
[30] D. Braga, I. G. Lezama, H. Berger, and A. F. Morpurgo, Nano Lett. **12**, 5218 (2012).
[31] Y. M. Zuev, W. Chang, and P. Kim, Phys. Rev. Lett. **102**, 096807 (2009).
[32] D. Sim, D. Liu, X. Dong, N. Xiao, S. Li, Y. Zhao, L.-J. Li, Q. Yan, and H. H. Hng, J. Phys. Chem. C **115**, 1780 (2011).
[33] Y. Nakai, K. Honda, K. Yanagi, H. Kataura, T. Kato, T. Yamamoto, and Y. Maniwa, Appl. Phys. Express **7**, 025103 (2014).
[34] K. Yanagi, S. Kanda, Y. Oshima, Y. Kitamura, H. Kawai, T. Yamamoto, T. Takenobu, Y. Nakai, and Y. Maniwa, Nano Lett. **14**, 6437 (2014).
[35] J. P. Fleurial, L. Gailliard, R. Triboulet, H. Scherrer, and S. Scherrer, J. Phys. Chem. Solids **49**, 1237 (1988).
[36] J. A. Wilson and A. D. Yoffe, Adv. Phys.**18**, 193 (1969).
[37] S. K. Srivastava and B. N. Avasthi, J. Mater. Sci. **20**, 3801 (1985).
[38] J. B. Patel, M. N. Parmar, M. P. Deshpande, G. K. Solanki, and M. K. Agarwal, Indian J. Pure & Appl. Phys. **43**, 527 (2005).
[39] G. K. Solanki, D. N. Gujarathi, M. P. Deshpande, D. Lakshminarayana, and M. K. Agarwal, Cryst. Res. Technol. **43**, 179 (2008).
[40] J.-Y. Kim, S. M. Choi, W.-S. Seo, and W.-S. Cho, Bull. Korean Chem. Soc. **31**, 3225 (2010).
[41] Y. Zhang, H. Li, L. Wang, H. Wang, X. Xie, S.-L. Zhang, R. Liu, and Z.-J. Qiu, Sci. Rep. **5**, 7938 (2014).
[42] X. Gu and R. Yang, Appl. Phys. Lett. **105**, 131903 (2014).
[43] W.-X. Zhou and K.-Q. Chen, Sci. Rep. **5**, 15070 (2015).
[44] R. Yan, J. R. Simpson, S. Bertolazzi, J. Brivio, M. Watson, X. Wu, A. Kis, T. Luo, A. R. H. Walker, and H. G. Xing, ACS Nano **8**, 986 (2014).
[45] A. Taube, J. Judek, A. Lapinska, and M. Zdrojek, ACS Appl. Mater. Interfaces **7**, 5061 (2015).
[46] C. Muratore, V. Varshney, J. J. Gengler, J. Hu, J. E. Bultman, A. K. Roy, B. L. Farmer, and A. A. Voevodin, Phys. Chem. Chem. Phys. **16**, 1008 (2014).
[47] M. Sledzinska, B. Graczykowski, M. Placidi, D. Saleta Reig, A. El Sachat, J. S. Reparaz, F. Alzina, S. Roche, B. Mortazavi, R. Quey, and C. M. Sotomayor Torres, arXiv:1604.04865.
[48] B. C. Wood, T. Ogitsu, M. Otani, and J. Biener, J. Phys. Chem. C **118**, 4 (2014).
[49] M. Otani and O. Sugino, Phys. Rev. B **73**, 115407 (2006).